Acta Crystallographica Section D
Biological Crystallography
ISSN 0907-4449

Structure of inorganic pyrophosphatase from *Helicobacter pylori*

Chun Ai Wu,[a] Neratur K. Lokanath,[a] Dong Young Kim,[a] Hye Jin Park,[a] Hye-Yeon Hwang,[a] Seong Tae Kim,[a] Se Won Suh[b] and Kyeong Kyu Kim[a]*

[a]Department of Molecular Cell Biology, Samsung Biomedical Research Institute, Sungkyunkwan University School of Medicine, Suwon 440-746, South Korea, and [b]Department of Chemistry, College of Natural Sciences, Seoul National University, Seoul 151-742, South Korea

Correspondence e-mail: kkim@med.skku.ac.kr

Received 21 January 2005
Accepted 11 August 2005

PDB Reference: *H. pylori* pyrophosphatase, 1ygz, r1ygzsf.

Inorganic pyrophosphatase (PPase) is a ubiquitous cytosolic enzyme which catalyzes the hydrolysis of inorganic pyrophosphate (PP_i) to orthophosphate (P_i). The crystal structure of inorganic pyrophosphatase from *Helicobacter pylori* (H-PPase) has been solved by MAD and refined to an R factor of 20.6% at 2.6 Å resolution. The crystallographic asymmetric unit contains a homohexameric H-PPase arranged as a dimer of trimers. While most of the structural elements of PPases are highly conserved in H-PPase, some unique structural features are localized in the flexible loops near the active site, suggesting that the structural flexibility of these loops is required for the catalytic efficiency of PPase.

1. Introduction

Inorganic pyrophosphatases (PPases; EC 3.6.1.1) are involved in energy metabolism *via* catalysis of the hydrolysis of inorganic pyrophosphate (PP_i), which yields inorganic orthophosphates (P_i; Chen *et al.*, 1990). As PP_i is a byproduct of numerous important biosynthetic reactions, including amino-acid and fatty-acid activation, nucleic acid polymerization and coenzyme synthesis, PPase shifts overall cellular equilibrium towards biosynthesis *via* the hydrolysis of PP_i (Lundin *et al.*, 1991). Because PPase plays such a vital role in biological metabolism, it is found ubiquitously in all organisms and its biological functions are quite well conserved (Sivula *et al.*, 1999).

Soluble PPases are divided into two families (families I and II) according to their primary structures. The two families of PPases share no sequence similarity and exhibit distinct catalytic mechanisms (Sivula *et al.*, 1999; Parfenyev *et al.*, 2001; Shintani *et al.*, 1998; Young *et al.*, 1998). In family I, all soluble PPases isolated to date manifest similar catalytic properties, but differ in regard to their oligomeric structures and in the size of their subunits. Most prokaryotic PPases form hexamers of 18–20 kDa, whereas eukaryotic enzymes tend to form homodimers of 30–35 kDa. Of the family I PPases, *Escherichia coli* PPase (E-PPase) is probably best characterized in terms of both biochemical and structural aspects (Kankare *et al.*, 1996; Salminen *et al.*, 1995; Cooperman, 1982; Ridlington *et al.*, 1972).

All known PPases require divalent metal ions for catalysis (Baykov *et al.*, 1996). Of the metal ions, magnesium confers the highest level of activity on PPase. An X-ray analysis of E-PPase in complex with magnesium ions revealed that four magnesium ions bound to the active site of PPase play dual roles in enzyme activation, as well as in recruiting the substrate as an $MgPP_i$ form (Kankare *et al.*, 1996). To date, four crystal structures have been reported for bacterial family

Table 1
Summary of data collection and refinement statistics of H-PPase.

Values in parentheses refer to the highest resolution shell.

	SeMet peak	SeMet inflection	SeMet remote
Data collection			
Space group	*P*3		
Unit-cell parameters (Å)	$a = b = 115.06$, $c = 73.78$		
No. of molecules in AU	6		
Wavelength (Å)	0.9797	0.9799	0.9740
Resolution (Å)	30.0–2.6 (2.69–2.6)	30.0–2.6 (2.69–2.6)	30.0–2.6 (2.69–2.6)
Completeness (%)	88.8 (88.1)	88.1 (87.9)	88.7 (88.4)
$R_{\rm merge}$† (%)	5.8 (35.9)	6.8 (34.5)	6.0 (33.7)
Observations	98225 (1161)	97137 (1159)	100142 (1132)
Unique reflections	29460 (2947)	29126 (2893)	29402 (2968)
Redundancy	3.3	3.3	3.4
$\langle I/\sigma(I)\rangle$	17.5 (2.8)	17.8 (3.0)	17.1 (2.8)
Refinement			
Resolution range (Å)	20.0–2.6		
No. of unique reflections	33036		
Completeness (%)	98.5		
R factor‡ (%)	20.6		
Free *R* factor (%)	26.5		
R.m.s.d. in bond lengths (Å)	0.01		
R.m.s.d. in bond angles (°)	1.2		

† $R_{\rm merge} = \sum_h \sum_i |I_{hi} 0\langle I_h\rangle|/\sum_h \sum_i I_{hi}$. ‡ R factor $= \sum_h |F_h^{\rm o} - F_h^{\rm c}|/\sum_h F_h^{\rm o}$.

I PPases: PPases from the mesophile *E. coli* (E-PPase; PDB code 1jfd; Avaeva *et al.*, 1997), from the thermophilic bacteria *Thermus thermophilius* (T-PPase; PDB code 2prd; Teplyakov *et al.*, 1994) and *Sulfolobus acidocaldarius* (S-PPase; PDB code 1qez; Leppanen *et al.*, 1999) and from the hyperthermophile *Pyrococcus horikishii* (P-PPase; PDB code 1ude; Liu *et al.*, 2004). Analyses of the crystal structures of apo PPases and their complexes with various metals and substrates have resulted in remarkable strides in our understanding of their structure–function relationships and reaction mechanisms. However, unanswered questions remain with regard to their catalytic activity and the evolutionary relationship between the PPases.

In order to characterize the general mechanisms underlying the catalytic cleavage of inorganic pyrophosphate by PPase, as well as the evolutionary relationships occurring among the members of this family of enzymes, we determined the crystal structure of PPase from *Helicobacter pylori* (H-PPase) at 2.6 Å resolution and compared its structure with those of other related PPases.

2. Materials and methods

2.1. Protein expression and crystallization

The gene encoding H-PPase, Hp0620, was amplified by PCR from the genomic DNA of *H. pylori* strain 26695 and cloned into a modified version of the pET21a(+) vector (Novagen) *via* the *Nde*I and *Xho*I restriction sites. Selenomethionine (SeMet) substituted protein was expressed in *E. coli* methionine-auxotroph strain B834 (DE3) cells (Stratagene). The cells were grown at 303 K in M9 medium containing ampicillin (50 µg ml^{-1}) to an A_{600} of 0.4–0.5 and then induced with 1 m*M* IPTG. Incubation then continued for 5 h. The cells were harvested by centrifugation for 10 min at 6000 rev min^{-1} and disrupted by sonication in 30 ml binding buffer (25 m*M* Tris–HCl pH 8.0, 0.5 *M* NaCl, 10 m*M* imidazole). The supernatant obtained after 45 min of centrifugation at 20 000 rev min^{-1} was applied onto a HiTrap chelating column (Amersham) equilibrated with binding buffer. The protein was eluted using a linear gradient of 0–0.5 *M* imidazole. The active fractions were collected and dialyzed against 25 m*M* Tris–HCl pH 8.5, 1 m*M* DTT, 0.1 *M* NaCl and applied onto a HiTrap Q column equilibrated with the same buffer. The protein was eluted with a linear gradient of 0–0.5 *M* NaCl in the same buffer. To further improve the purity of the protein, the concentrated protein was applied onto a Hi-Load Superdex-200 gel-filtration column (Amersham Pharmacia Biosciences, Sweden) equilibrated with buffer consisting of 50 m*M* Tris–HCl pH 7.0, 100 m*M* NaCl, 1 m*M* β-mercaptoethanol. The peak fractions from this elution were then pooled and concentrated to 14 mg ml^{-1} in the presence of 10 m*M* $MgCl_2$. The crystals were grown at 287 K by hanging-drop vapour diffusion against a reservoir solution containing 36%(*v*/*v*) MPD, 0.2 *M* $MgCl_2$ and 0.1 *M* imidazole at a pH of 8.0.

2.2. Data collection, structure determination and refinement

Multiple-wavelength anomalous diffraction (MAD) data sets were collected from a single crystal of the SeMet-substituted PPase at 100 K at the peak (0.9797 Å), edge (0.9799 Å) and remote (0.9740 Å) absorption wavelengths for selenium to 2.6 Å resolution at beamline 6B at the Pohang Accelerator Laboratory, South Korea. All diffraction images were processed using the *HKL* package (Otwinowski & Minor, 1997). The crystals were found to belong to a trigonal space group, with unit-cell parameters $a = b = 115.06$, $c = 73.78$ Å, $\alpha = \beta = 90$, $\gamma = 120^\circ$. *SOLVE*/*RESOLVE* was used to locate the three selenium sites and also for phasing and automated model building (Terwilliger & Berendzen, 1999, 2001). Phases were improved using the density-modification program *DM* (Cowtan & Main, 1998). 40% of residues were assigned with *RESOLVE* and the remaining residues were built manually using *QUANTA* (Accelrys, San Diego, CA, USA) with the help of the *CCP*4 suite (Collaborative Computational Project, Number 4, 1994). The structure was then subjected to rigid-body refinement with non-crystallographic symmetry (NCS) constraints using the *CNS* program (Brünger *et al.*, 1998). Each cycle of refinement with bulk-solvent and overall anisotropic *B*-factor corrections consisted of rigid-body refinement, simulated annealing incorporating the slow-cool protocol, positional refinement and *B*-factor refinement (individual or group). A complete model, including three SeMet residues in each monomer, was built during refinement using *CNS* (Brünger *et al.*, 1998). Initially, we processed the diffraction data set collected at the peak with an $R_{\rm merge}$ of 6.4% and refined the model in space group *P*321. However, the *R* failed to decrease during refinement ($R_{\rm free} = 36\%$). As trigonal space groups are prone to twinning,

we examined for twinning using the Twinning Server (http://www.doe-mbi.ucla.edu/Services/Twinning; Yeates, 1997) and detected perfect twinning. Additional refinement with twinning correction using the protocols from the section 'refinement with hemihedral twinning' of *CNS* (Brünger *et al.*, 1998) was unsuccessful. We then processed the data in space group *P*3, in which the crystal contains six molecules in an asymmetric unit with 62% solvent content. Successive refinement with twinning corrections in space group *P*3 yielded *R* and R_{free} values of 20.6 and 26.5%, respectively. The electron density was well defined for all residues except for the last residue and was continuous. Data-processing and refinement statistics are summarized in Table 1.

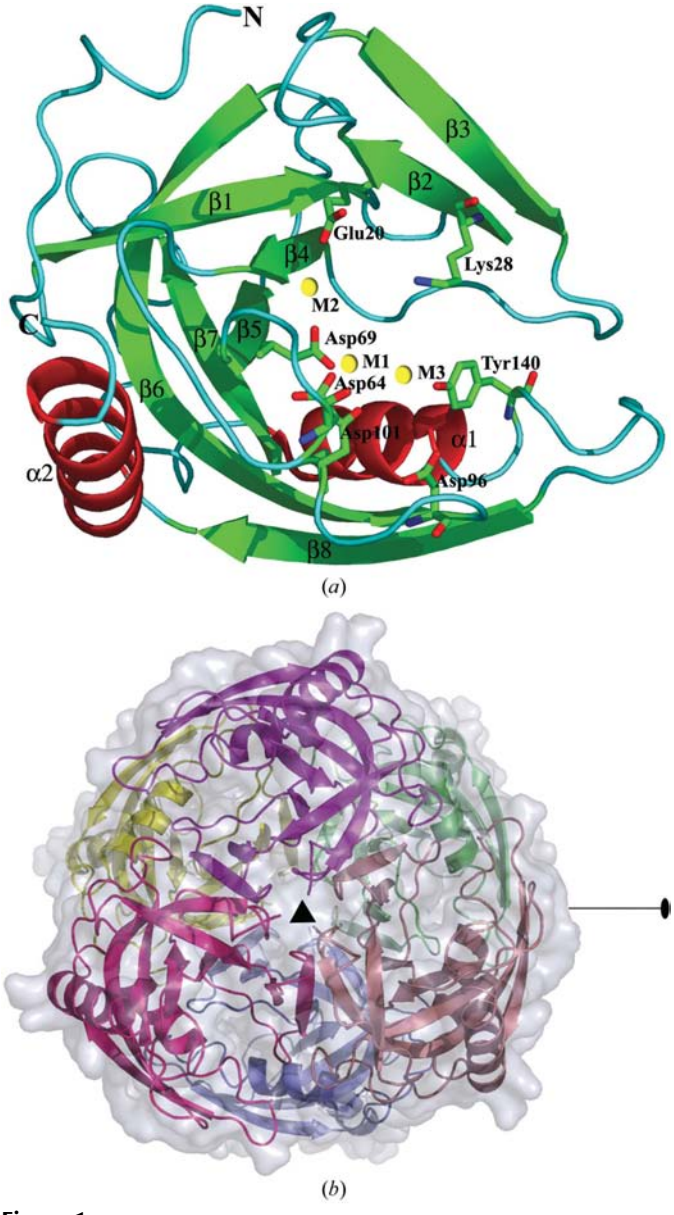

Figure 1
(*a*) Ribbon representation of the monomeric H-PPase produced with *PyMOL* (DeLano, 2002). β-Strands are labelled β1 to β8 and α-helices α1 and α2. The N- and C-termini are also labelled. The position of three strong peaks in the active centre are indicated by yellow balls labelled M1–M3 and the active-site residues involved in binding to the peaks are depicted as stick models. (*b*) Ribbon diagram and transparent surface representation of the hexameric assembly of H-PPase as viewed along the molecular threefold axis. Three subunits related by the noncrystallographic threefold axis are drawn in green, yellow and blue in one layer and pink, magenta and orange in the other layer. Molecular threefold and twofold axes are shown by a triangle and an oval, respectively.

2.3. Structure-based phylogenic tree

Crystal structures were aligned and alignment scores were calculated using the *FATCAT* server (Yuzhen & Adam, 2004). A score matrix was used to construct a phylogenic tree *via* the neighbour-joining method.

3. Results and discussion

3.1. Overall structure of H-PPase and its active site

The PPase from *H. pylori* (H-PPase) is composed of 173 amino-acid residues with a calculated molecular weight of 19 272 Da. Of the 173 H-PPase residues, we were able to model 172. The C-terminal residue could not be modelled, primarily because of weak electron density. H-PPase belongs to the $\alpha+\beta$ class of protein folds, with eight β-strands and two α-helices arranged in a β1-β2-β3-β4-β5-β6-β7-α1-β8-α2 topology (Fig. 1). In the centre of the PPase, five β-strands form an antiparallel β-barrel (strands 1, 4, 5, 6 and 7) surrounded by two α-helices (α1 and α2) and a long β-hairpin (β2 and β3). In H-PPase, the large cavity between the β-barrel and helix α1 constitutes the active site (Fig. 1*a*). In addition, helix α1 contributes to oligomeric contacts (Fig. 1*b*). 15 residues involved in binding to Mg^{2+} and PP_i are also conserved in H-PPase and are located in the active-site cavity (Fig. 2; Glu20, Lys28, Glu30, Arg42, Tyr50, Tyr54, Asp64, Asp66, Asp69, Asp96, Asp101, Lys103, Tyr140, Lys141 and Lys147). It has been suggested that PPases accommodate at least three magnesium ions, PP_i or 2 P_i (Bond *et al.*, 1980; Baykov *et al.*, 1989; Knight *et al.*, 1984). Three strong peaks located near the active site were identified in an $F_o - F_c$ electron-density map of H-PPase (Fig. 1*a*). Although magnesium ions are indistinguishable from water molecules in the electron-density map, these peaks are assumed to be the magnesium ions because they are localized at the metal-binding sites *M*(I), *M*(II) and *M*(III) and make hydrogen bonds with Glu20, Asp64, Asp69, Asp96 and Asp101, all of which are known to bind metal ions (Heikinheimo *et al.*, 1996) (Fig. 1*a*). The additional water peak found in the active site of H-PPase may be assigned in the phosphate site, making hydrogen bonds with Lys28 and Tyr140. These results imply that H-PPase operates *via* the same general catalytic mechanisms as do other family I PPases.

3.2. Oligomeric structure

As observed in other bacterial PPases (Avaeva *et al.*, 1997; Teplyakov *et al.*, 1994; Leppanen *et al.*, 1999; Liu *et al.*, 2004), H-PPase forms a homohexamer arranged into a dimer of trimers (Fig. 1*b*). In the *P*3 space group, one hexameric H-PPase is found in the asymmetric unit. Each subunit contains residues 1–172 of the total 173 residues. As the

Table 2
Accessible surface areas of bacterial PPases (Å^2).

	Hexamer	Monomer†	Hexamer/monomer	Buried surface area‡
H-PPase	39879	8837	4.51	13143
E-PPase	41111	8969	4.58	12705
S-PPase	38629	8675	4.45	13421
T-PPase	38277	8774	4.36	14368
P-PPase	38490	8957	4.29	15255

† Average surface area of six monomers in each hexameric oligomer. ‡ Buried surface areas are calculated by subtracting the surface area of the hexamer from the surface areas of six monomers.

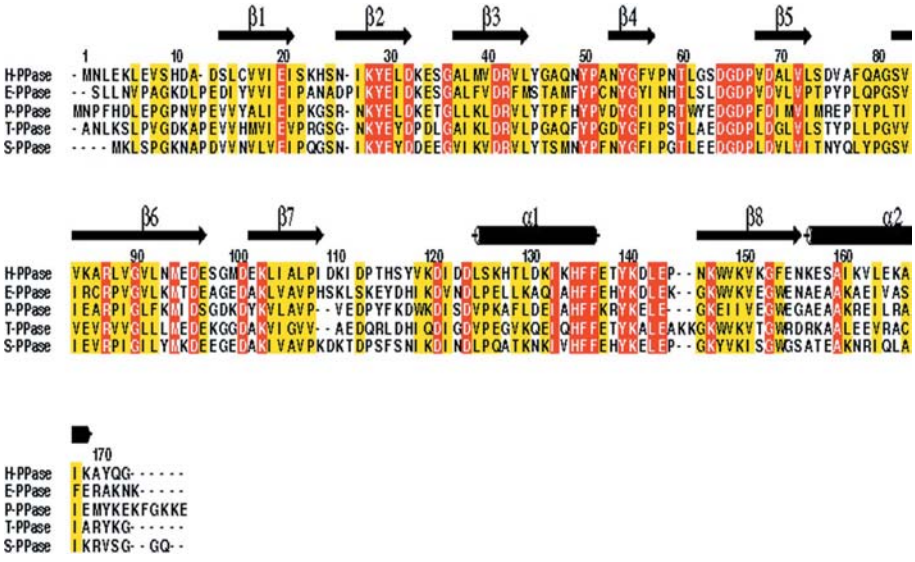

Figure 2
Multiple sequence alignment of H-PPase with other homologous PPases: E-PPase from *E. coli* (PDB code 1jfd; Kankare *et al.*, 1996), P-PPase from *P. horikoshii* (PDB code 1ude; Leppanen *et al.*, 1999), T-PPAse from *T. thermophilus* (PDB code 2prd; Avaeva *et al.*, 1997) and S-PPase from *S. acidocaldarius* (PDB code 1qez; Teplyakov *et al.*, 1994). Secondary-structure elements and residue numbers are shown for H-PPase. 15 residues conserved in the active-site cavity are indicated by asterisks (*). In the alignment, identical residues are boxed in red and homologous residues are boxed in yellow.

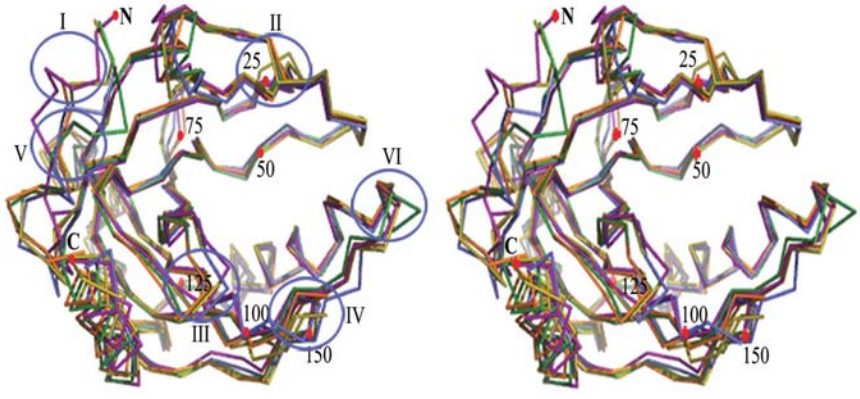

Figure 3
Superposition of members of the family I PPases in the same orientation as the H-PPase in Fig. 1(*a*). C$^\alpha$ atoms of H-PPase (purple), E-PPase (olive), T-PPase (forest), S-PPase (orange) and P-PPase (slate) are used in the superposition. The N- and C-termini and every 25th residue are indicated by red balls and labelled. Structurally divergent regions are indicated by black ovals and labelled I, II, III, IV, V and VI.

diffraction data of H-PPase can be scaled in the *P*321 space group with a low R_{sym} value [$R_{sym}(P321)$ = 6.4% compared with $R_{sym}(P3)$ = 5.9%], it is expected that the non-crystallographic twofold symmetry is very similar to the crystallographic symmetry. Indeed, the two trimers can be superimposed with a root-mean-square deviation (r.m.s.d.) of 0.2 Å for 316 C$^\alpha$ atoms. The tight packing observed among the hexameric subunits of H-PPase is also seen in other PPases (Avaeva *et al.*, 1997; Teplyakov *et al.*, 1994; Leppanen *et al.*, 1999; Liu *et al.*, 2004), suggesting functional significance of the tight assembly. As the oligomerization of PPase is known to be essential for its stability (Avaeva *et al.*, 1997), it could be postulated that the tight packing in the hexamer, or the burial of a large surface area upon oligomerization, is important with regard to the thermostability of PPase. Of the PPases isolated from the five archaebacteria or eubacteria compared in this paper, the PPases from thermophilic organisms (T-PPase and S-PPase) appear to form tighter assemblies than the PPases from mesophiles (E-PPase and H-PPase), largely because the buried surface areas of the oligomeric PPases are larger for the thermophiles than they are for the mesophiles (Table 2). Moreover, the buried binding surface is maximized in the PPase from the hyperthermophilic organism (P-PPase in Table 2). These findings suggest that the tight oligomeric packing is directly related to the thermostability of PPases, which is consistent with previous reports (Leppanen *et al.*, 1999; Liu *et al.*, 2004).

3.3. Structural comparison with other PPases and evolutionary relationship

The structure of the H-PPase subunit and its hexameric assembly are similar to those of all other PPases whose structures have been determined to date (Fig. 3). The monomer of H-PPase is found to overlap with those of the other four PPases, with r.m.s.d. values ranging from 1.0 to 1.4 Å for 169 C$^\alpha$ atoms. Structural divergences are found in the N-terminal region, as well as in several loop regions (I, II, III, IV V and VI in Fig. 3), while the core region appears to be very well conserved. The structural differences observed in the loops between β1 and β2 ('II' in Fig. 3), between β7 and α1 ('V' in Fig. 3) and between α1 and β8 ('VI' in Fig. 3) arise

Table 3
Sequence identities (%) and r.m.s.d.s (Å) of crystal structures of bacterial PPases.

Identities (%) are given below the diagonal and r.m.s.d.s (Å) above. 169 C^{α} atoms of the PPases monomer were used for structural superposition to calculate the r.m.s.d.

	H-PPase	E-PPase	S-PPase	T-PPase	P-PPase
H-PPase	–	1.3	1.2	1.0	1.3
E-PPase	45.45	–	1.0	1.3	1.4
S-PPase	47.43	50.57	–	1.0	1.1
T-PPase	44.32	46.63	47.19	–	0.8
P-PPase	38.67	41.21	46.96	42.54	–

from the insertion or deletion of residues (Figs. 2 and 3). The loop between β1 and β2 of H-PPase is similar in length to the loops found in T-PPase, S-PPase and P-PPase, but is shorter than the loop in E-PPase. The loop found between β7 and α1 is similar to the loops found in E-PPase and S-PPase, but is quite different from the loops in P-PPase and T-PPase. Additionally, the loop between α1 and β8 is similar to the loops in E-PPase and S-PPase, but differs from the loops found in P-PPase and T-PPase. Other loops which exhibit significant structural differences among PPases are generally located near the active site (III, IV and V), suggesting that such structural flexibility may be related to the enzymatic activity of PPases. Interestingly, it has been revealed that structurally divergent regions exhibit high temperature factors (Fig. 4). In some aspects, structural divergence may be interpreted as the result of model error. However, as the evolutionary conservation of disordered structural elements might reflect their flexibility for PPase catalysis (Moiseev *et al.*, 2004), the flexibilities of the loops may also be correlated with the conformational changes of PPase, as well with as the uptake of substrate into the active site. In fact, mutants with decreased flexibility in these loops ('IV' and 'VI' in Figs. 3 and 4) manifested decreased catalytic activity. Therefore, we conclude that the overall structure of PPases is well conserved, with the exception of the loop regions covering the active site. However, the conformational divergence of these loops

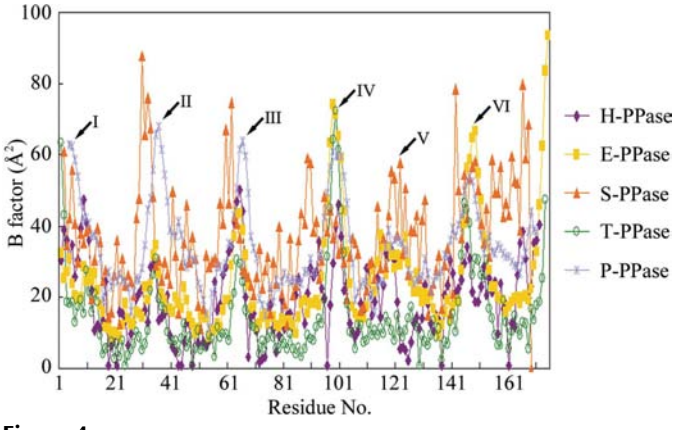

Figure 4
The *B* factors of H-PPase (purple), E-PPase (yellow), T-PPase (green), S-PPase (orange) and P-PPase (light blue) are plotted against the amino-acid residue number. Flexible regions with high *B* factors are indicated by I, II, III, IV, V and VI.

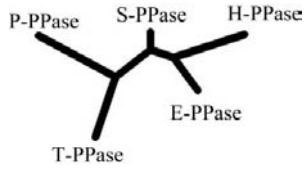

Figure 5
Phylogenic tree of five bacterial PPases based on structural alignment of hexameric H-PPase, E-PPase, T-PPase, S-PPase and P-PPase.

reflects structural flexibility, which is a characteristic feature of PPase. These observations, when taken together, suggest that evolutionarily PPases are quite well conserved with regard to functional aspects as well as structural aspects.

H-PPase shares high sequence and structural homologies with other PPases (Table 3). The phylogenic tree of family I PPases based on sequence alignment reveals that H-PPase is evolutionarily close to E-PPase and S-PPase, but relatively unrelated to T-PPase and P-PPase (see Fig. 2 in Sivula *et al.*, 1999). However, this evolutionary relationship is not consistent with the structural homologies exhibited when the subunit structures of the PPases are compared. In the case of subunit homology, H-PPase exhibits maximum structural similarity to T-PPase and minimum similarity to E-PPase (Table 3). However, when the structures of the hexameric PPases are analyzed, rather than those of the monomeric PPases, their evolutionary relationships appear to be well conserved, as both sequence-based and structure-based phylogenic trees are almost identical (see Fig. 2 in Sivula *et al.*, 1999, and Fig. 5). As PPase functions as a hexameric assembly rather than a monomer, it is reasonable to conclude that structural conservation would also be observed in the hexameric assembly of PPase.

4. Conclusions

In this report, we solved the three-dimensional crystal structure of PPase from *H. pylori* and compared its structure with the established crystal structures of PPases from eubacteria and archaebacteria. H-PPase exhibited general structural and functional properties that were the same as those of other PPases. *Via* structural comparison, we were able to confirm that structural diversity is found in the loops located near the active site, suggesting that the flexible nature of the loops necessary for the catalytic efficacy of PPase is conserved among family I PPases. In addition, structural comparison of hexameric PPases appears to reflect the evolutionary relationship between PPases from bacterial species.

This work was supported by grant No. FG03-31-02 from the 21C Frontier Functional Human Genome Project of the Ministry of Science and Technology of Korea. Experiments at PLS were supported in part by MOST and POSCO.

References

Avaeva, S., Kurilova, S., Nazarova, T., Rodina, E., Vorobyeva, N., Sklyankina, V., Grigorjeva, O., Harutyunyan, E., Oganessyan, V.,

Wilson, K., Dauter, Z., Huber, R. & Mather, T. (1997). *FEBS Lett.* **410**, 502–508.
Baykov, A. A., Hyytia, T., Valk, S. E., Kasho, V. N., Vener, A. V., Goldman, A., Lahti, R. & Cooperman, B. S. (1996). *Biochemistry*, **35**, 4655–4661.
Baykov, A. A., Shestakov, A. S., Pavlov, A. R., Smirnova, I. N., Larionov, V. N. & Avaeva, S. M. (1989). *Biokhimiya*, **54**, 796–803.
Bond, M. W., Chiu, N. Y. & Cooperman, B. S. (1980). *Biochemistry*, **19**, 94–102.
Brünger, A. T., Adams, P. D., Clore, G. M., DeLano, W. L., Gros, P., Grosse-Kunstleve, R. W., Jiang, J.-S., Kuszewski, J., Nilges, M., Pannu, N. S., Read, R. J., Rice, L. M., Simonson, T. & Warren, L. (1998). *Acta Cryst.* D**54**, 905–921.
Chen, J., Brevet, A., Formant, M., Leveque, F., Schmitter, J. M., Blanqust, S. & Plateau, P. (1990). *J. Bacteriol.* **172**, 5686–5689.
Collaborative Computational Project, Number 4 (1994). *Acta Cryst.* D**50**, 760–763.
Cooperman, B. S. (1982). *Methods Enzymol.* **87**, 526–548.
Cowtan, K. & Main, P. (1998) *Acta Cryst.* D**54**, 487–493.
DeLano, W. L. (2002). *The PyMOL Molecular Graphics System.* http://www.pymol.org.
Heikinheimo, P., Lehtonen, J., Baykov, A., Lahti, R., Cooperman, B. S. & Goldman, A. (1996). *Structure*, **4**, 1491–1508.
Kankare, J., Salminen, T., Lahti, R., Cooperman, B. S., Baykov, A. A. & Goldman, A. (1996). *Biochemistry*, **35**, 4670–4677.
Knight, W. B., Dunaway-Mariano, D., Ranson, S. C. & Villafranca, J. J. (1984). *J. Biol. Chem.* **259**, 2886–2895.
Leppanen, V. M., Nummelin, H., Hansen, T. & Lahti, R. (1999). *Protein Sci.* **8**, 1218–1231.
Liu, B., Bartlam, M., Gao, R., Zhou, W., Pang, H., Liu, Y., Feng, Y. & Rao, Z. (2004). *Biophys. J.* **86**, 420–427.
Lundin, M., Baltscheffsky, H. & Ronne, H. (1991). *J. Biol. Chem.* **266**, 12168–12172.
Moiseev, V., Rodina, E. & Kurilova, S. A. (2004). *Eur. J. Biochem.* **271**, *Suppl.* 1, 80 (Abstract P3.2–43).
Otwinowski, Z. & Minor, W. (1997). *Methods Enzymol.* **276**, 307–326.
Parfenyev, A. N., Salminen, A. N., Halonen, P., Hachimori, A., Baykov, A. A. & Lahti, R. (2001). *J. Biol. Chem.* **276**, 24511–24518.
Ridlington, J. W., Yang, Y. & Butler, L. G. (1972). *Arch. Biochem. Biophys.* **153**, 714–725.
Salminen, T., Kapyla, J., Heikinheimo, P., Kankare, J., Goldman, A., Heininen, J., Baykov, A. A., Cooperman, B. S. & Lahti, R. (1995). *Biochemistry*, **34**, 782–791.
Shintani, T., Uchiumi, T., Yonezawa, T., Salminen, A., Baykov, A. A., Lahti, R. & Hachimori, A. (1998). *FEBS Lett.* **439**, 263–266.
Sivula, T., Salmine, A., Parfenyev, A. N., Pohjanijoki, P., Goldman, A., Cooperman, B. S., Baykov, A. A. & Lahti, R. (1999). *FEBS Lett.* **454**, 75–80.
Teplyakov, A., Obmolova, G., Wilson, K. S., Ishii, K., Kaji, H., Samejima, T. & Kuranova, I. (1994). *Protein Sci.* **3**, 1098–1107.
Terwilliger, T. C. & Berendzen, J. (1999). *Acta Cryst.* D**55**, 849–861.
Terwilliger, T. C. & Berendzen, J. (2001). *Acta Cryst.* D**57**, 1755–1762.
Yeates, T. O. (1997). *Methods Enzymol.* **276**, 344–358.
Young, T. W., Kuhn, N. J., Wadeson, A., Ward, S., Burges, D. & Cooke, G. D. (1998). *Microbiology*, **144**, 2563–2571.
Yuzhen, Y. & Adam, G. (2004). *Nucleic Acids Res.* **32**, 582–585.